Hindawi
Scientific Programming
Volume 2022, Article ID 6057641, 10 pages
https://doi.org/10.1155/2022/6057641

Research Article

Study on Simulation Law of Cuttings Migration in Shale Gas Horizontal Wells

Ye Chen,[1] Youcheng Zheng,[2] Bo Zeng,[1] Yu Fan,[3] Pengcheng Wu,[1] Xudong Wang,[1] and Chengyu Xia[4]

[1]*Shale Gas Research Institute of Petro China Southwest Oil and Gas Field, Chengdu, Sichuan 610051, China*
[2]*PetroChina Southwest Oil and Gas Field Company, Chengdu, Sichuan 610051, China*
[3]*Engineering Technology Research Institute, PetroChina Southwest Oil and Gasfield Company, Chengdu 610031, China*
[4]*School of Mechanical Engineering, Yangtze University, Jingzhou, Hubei 434000, China*

Correspondence should be addressed to Chengyu Xia; qlq1010@126.com

Received 7 April 2022; Revised 30 May 2022; Accepted 3 June 2022; Published 14 July 2022

Academic Editor: Punit Gupta

Inland and offshore oil exploitation, large displacement, and horizontal well are more and more widely used, which can significantly improve the oilfield exploitation efficiency and economic benefits. However, in the complex drilling process, the debris particles generated in the large displacement and horizontal well section drilling are deposited in the lower low-speed area of the lower part of the ring empty shaft. It will cause underground accidents such as complex moving, drilling, increased resistance, drilling column fracture, and so on, which will seriously affect the efficiency and economic benefits of drilling. This paper addresses the problem of annular debris accumulation and the characteristics of high-density drilling fluid and uses the CFD-DEM (discrete cell method) method to simulate the debris movement process in the well eye based on the coupling of FLUENT and EDEM software. The edge calculation is used to provide strong resource allocation and calculation force support for this paper, fully consider the influence of the interaction between drilling fluid, debris particles, and drilling rod and well wall, and explore the influence law of the eccentric ring space of the conventional steel drill pipe.

1. Introduction

The drill bit produces much rock debris, carried by drilling fluid into the ring space in rock breaking. Many domestic scholars have done a lot of research on the influencing factors of rock debris movement inside the empty ring.

Huque et al. [1] established a three-layer unstable chip transport model based on a three-layer and two-layer unstable model. They analyzed the suspension, rolling, and sliding mechanism and solid and liquid relative speed in the suspension layer. Amanna et al. [2] used CFD and experiments to study the influence of fluid flow, drill rod rotation, particle cutting size, and well slope angle on the movement behavior of rock debris and found that the well slope between 45 and 60° was the most difficult to clean. Oseh et al. [3] used composite water-based mud (WBM) to study the influence of different drilling parameters on rock transport efficiency, and PP-SiO2-NC composite WBM showed good performance during rock transport. Zhang et al. [4] elaborated on the experimental research purpose, classification of influencing factors, and experimental observation of flow type and summarized the influence law of the main research factors on rock debris movement in the experiment, which provided a basis for the next research. Xiang et al. [5] established the rock carrying experimental device of large displacement horizontal well through a similar theory. They studied the changing relationship between various drilling parameters and the thickness of irrational debris bed, which has reference significance for purifying the minimum rock carrying displacement and optimizing the mechanical drilling speed. Benyounes et al. [6] compared the errors of numerical simulation and actual critical velocity and corrected the mathematical model of a horizontal well, which laid a theoretical foundation for meeting the needs of field

construction drilling design. Sorgun et al. [7] used computational fluid mechanics (CFD) and support vector regression (SVR) methods to predict pressure losses in newtonian and nonnewtonian fluids in concentric horizontal torian space. Mohammadreza et al. [8] simulated the debris migration process of continuous technology (CTT) through experiments and the Euler particle method and studied the influence of different parameters on debris migration. To consider the collision phenomenon of the particles, Akhshik et al. [9] coupled the CFD and DEM to study the influence of the liquid flow, the air injection volume, the air inclination, the temperature and pressure on the rock chip transport efficiency, and the simulation prediction results are in good agreement with the experimental data. Zhai et al. [10] analyzed the influence of gas-liquid accumulation flow ratio, drill rotation, and eccentricity on debris movement. It is believed that the liquid phase flow plays the dominant role, the gas-liquid accumulation flow ratio is relatively small, and the rotating drill rod is conducive to the movement of rock debris.

Through the above investigation, it can be seen that the well hole cleaning is mainly concentrated on the mechanical debris cleaning tool, and the rock debris structure carries the debris particles into the upper loop by enhancing the turbulence strength of the surrounding flow field to improve the migration efficiency of the debris. Although enhancing the turbulence strength of the flow field can carry the debris in the upper loop space high-speed area in a short distance, the scope of the debris cleaning device is limited. The large slope and horizontal well depth are very long when part of the debris cleaning tool to the upper loop, the debris particles did not reach the highway area will fall back to the bottom of the shaft to form the debris bed. Secondly, because the debris particles are easy to bond in the mechanical blade debris cleaning tool gap, it is easy to form a mud package, reducing the debris cleaning effect. Therefore, the study of horizontal shale wells can provide feasibility suggestions for debris clearing.

2. The CFD-DEM Coupling of the Basic Governing Equations

2.1. Governing Equation

2.1.1. Continuity Equation

$$\frac{\partial}{\partial_t}\left(\alpha_f \rho_f\right) + \nabla.\left(\alpha_f \rho_f v_f\right) = 0 \tag{1}$$

2.1.2. Momentum Conservation Equation

$$\frac{\partial}{\partial t}\left(\alpha_f \rho_f u_i\right) + \frac{\partial}{\partial x_j}\left(\alpha_f \rho_f u_i u_j\right) = -\frac{\partial p}{\partial x_i} + \frac{\partial}{\partial x_j}\left[\alpha_f \mu_{eff}\left(\frac{\partial u_i}{\partial x_j} + \frac{\partial u_j}{\partial x_i}\right)\right] + \alpha_f \rho_f g + F_s,$$

$$\alpha_f = 1 - \sum_{i=1}^{m} \frac{V_{pi}}{V_{\text{cell}}}, \tag{2}$$

where ρ_f is density of drilling fluid, kg/m^3; α_f is drilling fluid volume fraction; v_f is drilling fluid speed, m/s; τ is drilling fluid shear stress, p_a; S_f is fluid particle interaction force, N; g is acceleration of gravity, m/s^2; V_{pi} is the volume of the debris particles i; V_{cell} is the volume of the calculated unit; $F_{f,i}$ is the drag force of the individual particles, N; and m is total number of particles within the cell.

2.1.3. Turbulence Equation

$$\frac{\partial}{\partial_t}\left(\rho_f k\right) + \frac{\partial}{\partial_{x_j}}\left(\rho_f k \mu_j\right) = \frac{\partial}{\partial_{xj}}\left(\alpha_k \mu_{eff} \frac{\partial k}{\partial x_j}\right) + G_k + G_b - \rho_f \varepsilon - Y_M + S_k,$$

$$\frac{\partial}{\partial_t}\left(\rho_f \varepsilon\right) + \frac{\partial}{\partial_{x_j}}\left(\rho_f \varepsilon \mu_i\right) = \frac{\partial}{\partial_{xj}}\left(\alpha_\varepsilon \mu_{eff} \frac{\partial \varepsilon}{\partial x_j}\right) + C_{1\varepsilon}\frac{\varepsilon}{k}\left(G_k + C_{3\varepsilon} G_b\right) - C_{2\varepsilon}\rho_f \frac{\varepsilon^2}{k} - R_\varepsilon + S_\varepsilon, \tag{3}$$

where k is chuai kinetic energy, m^2/s^2; ε is turbulence dissipation, m^2/s^2; μ_{eff} is power viscosity coefficient, $kg/m.s$; μ_j is turbulence viscosity coefficient, $kg/m.s$; μ_i is time averaged velocity, m/s; G_k is turbulent kinetic energy resulting from a laminar velocity gradient, J; G_b is turbulent kinetic energy generated by buoyancy, J; Y_{k} and Y_ω is turbulence generated by the diffusion; and α_k and α_ε is turbulence plant number of equation k and ω.

2.1.4. Fluid Force on the Particles.

$$F_{bi} = -V_{pi}\nabla P,$$

$$F_d = \beta\left(v_f - v_p\right),$$

$$\beta = \begin{cases} \dfrac{\mu\left(1-\alpha_l\right)}{d_p^2 \alpha_l}\left[150\left(1-\alpha_l\right) + 1.75 R_{e_p}\right] & \left(\alpha_l \le 0.8\right), \\ \dfrac{3}{4} C_D \dfrac{\mu\left(1-\alpha_l\right)}{d_p^2}\alpha_l^{-2.65} & \left(\alpha_l > 0.8\right), \end{cases}$$

$$C_D = \begin{cases} \dfrac{24\left(1 + 0.15 R_{e_p}^{0.687}\right)}{R_{e_p}} & \left(R_{e_p} \le 1000\right). \\ 0.44 & \left(R_{e_p} > 1000\right), \end{cases} \tag{4}$$

where reynolds number R_{e_p} is $R_{e_p} = \rho_l \alpha_l d_p |v_f - v_p|/\mu$; d_p is particle diameter, mm; v_f is fluid speed, m/s; v_p is particle speed, m/s; α_l is particle space rate; and μ is fluid shear viscosity.

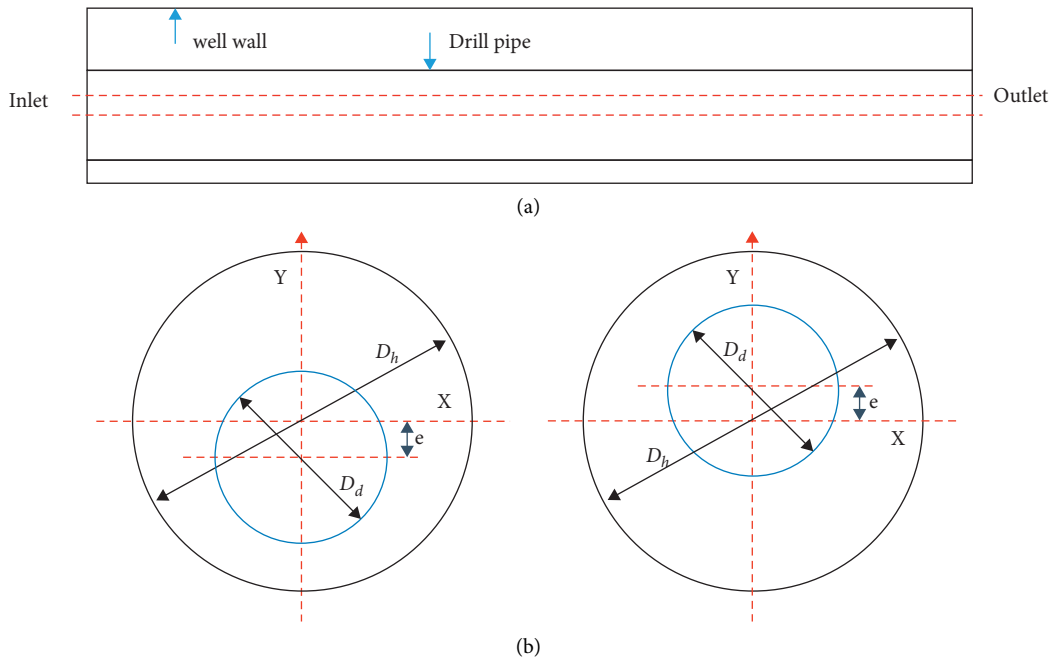

Figure 1: Geometric model of annulus: (a) model axial diagram; (b) negative eccentric; (c) positive eccentric.

2.1.5. Drilling Rheology

$$\tau = k\gamma^n,$$
$$n = 3.321 \log\left(\frac{\varphi 600}{\varphi 300}\right), \quad (5)$$
$$k = \frac{0.511\varphi 300}{511^n},$$

where τ is shear stress; k is drilling fluid consistency coefficient, Pa · s; n is drilling fluidity index; φ#x2009; 600 is registration of the drilling fluid at 600 rpm, andφ300 is registration of the drilling fluid at 300 rpm, as shown in Figure 1.

2.2. Geometric Model. The 3 D model is established according to the horizontal well combination parameters. Since the actual large obliquity and horizontal well length cannot be simulated, the length of the simulated shaft is 5 m and 103 mm, and the shaft diameter is 203.2 mm. The schematic diagram of the model is shown in figure 2(a). Due to the dead weight of the drill pipe, the drill is below the lower part of the ring, but the actual eccentric position is difficult to determine. Therefore, this paper represents the degree of drill eccentricity by eccentricity. The direction is determined according to the modeling coordinates. If the drill rod is sunk, a negative eccentricity appears (Figure 2(b)); if the drill rod is floating and the drill rod is in the upper part of the ring space, a positive bias appears. The eccentricity formula is calculated as follows:

$$\varepsilon = \frac{2e}{D_h - D_d}, \quad (6)$$

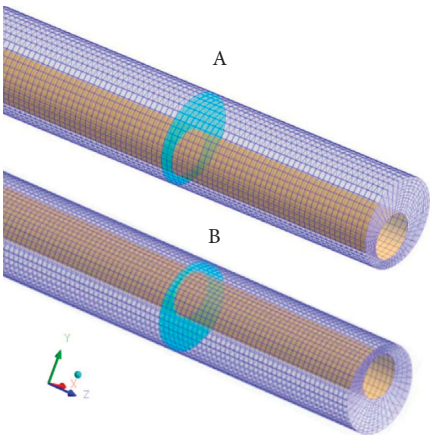

Figure 2: Geometric model of annulus.

where ε is drill eccentricity; e is the distance of the shaft center to offset the center of the shaft, mm; D_h is the diameter of the well eye, mm; andD_d is drill diameter, mm.

The traditional steel drill rod models are eccentric and long straight pipes. To improve the accuracy of computation and simulation, the hexahedral mesh should be selected to divide the mesh division method. Furthermore, the # 1 grid division method is used to divide the grid.

The model contact parameters presented in this paper are shown in Table 1. To simulate the continuous entry of actual debris particles, the geometric model entrance is considered as a virtual inlet (Virtual). Simply put, when setting the inlet conditions, only the entry of particle mass is considered, and the porosity between particles and other factors are not considered. Due to the certain mechanical drilling speed during the drilling process, the particle mass

Table 1: Basic parameters.

Parameter	Name	Simulation values	Unit
D_h	The diameter of the well eye	203.2	mm
D_d	Drill diameter	103	mm
L	Length of drill pipe	5	m
ρ_p	Density of rock debris	2600	kg/m3
ρ_f	Density of drilling fluid	1920	g/cm3
d_p	Diameter of rock debris	1, 2, 3, 4	mm
u_o	Drilling fluid displacement	20, 25, 30, 35, 40	L/s
ω	Bull rod rotation rate	40, 60, 80, 100, 120	rpm
ε	Eccentricity	0, 0.2, 0.4, 0.6	--

Table 2: Contact parameters of the model.

Rock fragment parameters	Density (kg/m^3)	2600	
	Young modulus	15000	
	Poisson ratio	0.25	
Rock contact mechanics model	Interface	Rock debris and rock debris	Rock debris and wall surface
	Static friction coefficient	0.61	0.7
	Coefficient of rolling friction	0.01	0.02
	Elastic recovery coefficient	0.5	0.5

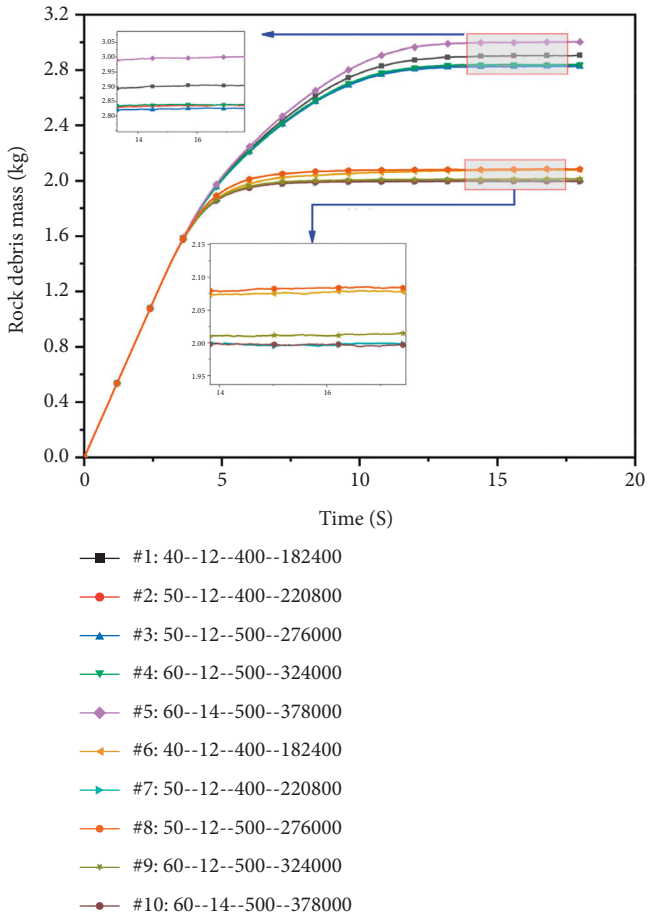

Figure 3: The mass of cuttings in annulus varies with the total mesh number.

Table 3: Other parameters settings.

Output volume (L/s)	Grain size (mm)	Eccentricity	Rock fragments inlet rate (kg/s)
30 L/s	3	−0.6	0.45

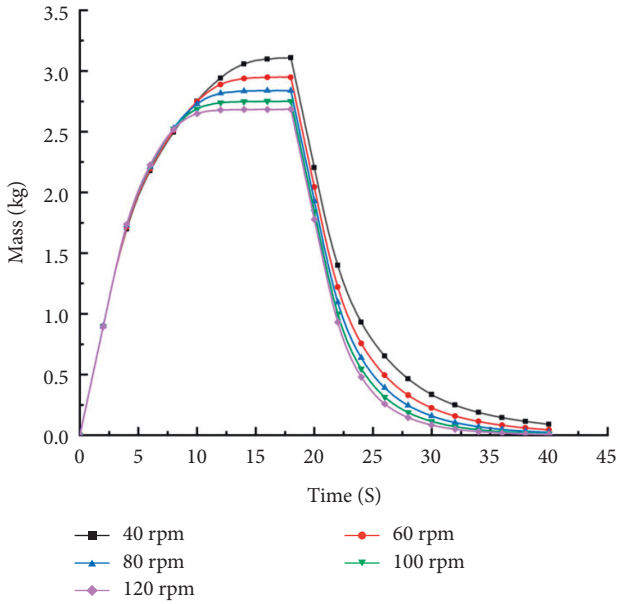

Figure 4: Curve of cuttings quality change at different rotating speeds.

flow injection is set at the inlet, regardless of the porosity between the particles. Table 2.

Due to the many factors affecting drilling parameters, the following parameters are considered, and the specific simulation parameters are shown in Table 1.

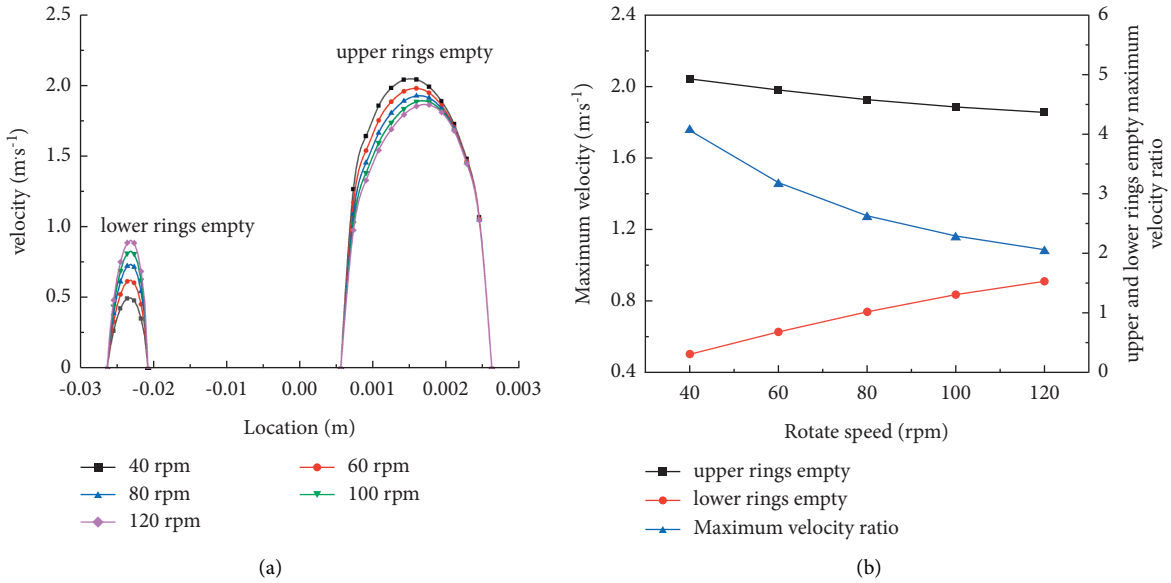

Figure 5: Curve of fluid velocity change at different rotating speeds: (a) the axial velocity of the fluid; (b) maximum fluid velocity and its ratio.

$$Q_m = \frac{\pi (D_h/2)^2 \times ROP \times \rho_p}{3600}. \quad (7)$$

where Q_m is mass flow rate of rock debris particles, kg/s, D_h is the diameter of the well eye, ROP is rate of penetration, m/s, and ρ_p is density of debris particles, kg/m^3.

2.3. Grid-Independent Validation. As appears in Figure 3, after changing the total number of grids, the total debris mass calculated by the conventional steel drill model fluctuates between 2.83 kg and 3.01 kg. The total debris mass calculated by the new aluminum alloy drill rod model fluctuates between 1.99 kg and 2.01 kg, verifying the grid independence and indicating good convergence. According to the enlarged figure in Figure 3, since the total debris mass fluctuation of # 1 and # 9 is in the median value, the # 1 grid division method is used for the traditional steel drill rod model below. In comparison, the # 9 grid division method is used for the new aluminum alloy drill rod model.

3. Results and Discussion

3.1. Effect of Drill Speed on Debris Movement. The speed of the drill rod is one of the critical factors affecting well hole debris settlement and well purification, and the rock carrying capacity and purification ability of drilling rods of different speeds are also different. To study the relationship between debris deposition quality, purification time, and drill rod speed in the borehole ring, this section simulates the effect on the settlement of rock debris in the bore at speeds of 40 rpm, 60 rpm, 80 rpm, 100 rpm, and 120 rpm, respectively. Other parameter settings are shown in Table 3.

Figure 4 shows the debris deposition mass and well hole purification time at different rotational speeds. In the drilling process, with the gradual increase of the drill rod drilling speed, the curve slope of the linear stage of the debris settlement is the same, but the faster the debris mass curve slope decreases in the transition settlement stage, the faster the corresponding time enters the dynamic stability stage. This shows that increasing the speed of the drill pipe has a significant role in improving the rock carrying efficiency and makes the bore enter the dynamic stability stage quickly, which is conducive to improving the stability.

When the drill bit stops drilling operation for reverse cycle operation, the rock debris injection is stopped at 18 seconds, the curve slope of the linear discharge stage of the rock bit is the same at different speeds, but in the excessive discharge stage, with the gradual reduction of the drilling speed, the longer the well purification consumes. It shows that

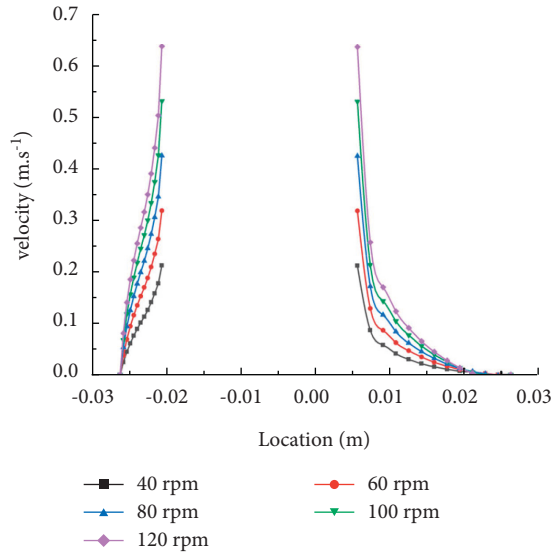

Figure 6: Variation curve of tangential velocity of fluid at different rotating speeds.

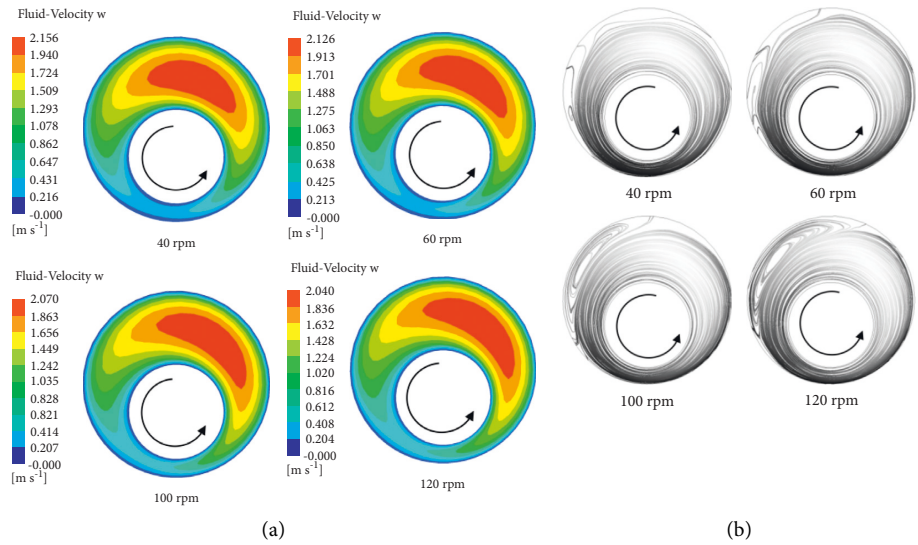

Figure 7: Cloud diagram of fluid velocity at different rotations: (a) speed cloud map; (b) streamlined diagram.

Table 4: Other parameters settings.

Rotation rate (rpm)	Grain size (mm)	Eccentricity	Debris inlet flow rate (kg/s)
80	3	−0.6	0.45

increasing the rotation speed of the drill bore is beneficial to improving the efficiency of debris movement, reducing the debris amount and purification time in the well eye, and accelerating the stability of the flow field in the well eye.

When the shaft ring air reaches dynamic stability at 18 s, take the vertical symmetry axis deviation of 15 on the loop air section to pass through the highest and lowest flow rate zone. Then, the axial and tangential flow rates of the fluid on the intercept line are then extracted separately (the following subsections are all this method). From the axial velocity distribution curve of the ring air at different speeds(Figure 5(a)), it can be seen that there is a velocity difference between the upper and lower rings empty, and the upper annular velocity decreases with the rotation speed, while the lower loop gradually increases. The maximum flow velocity curve of figure 5(b) shows that the upper and lower rings' empty maximum velocity ratio decreases. It shows that the axial speed of the lower annular drilling fluid increases with the rotation speed of the drilling column, which reduces the speed difference between the two and accelerates the movement of rock debris to the wellhead.

Figure 6 shows the tangential velocity distribution curve in the ring air at different rotational speeds. It can be seen that the tangential velocity of the drilling fluid in the ring air increases with the rotation velocity of the drill column, and the tangential velocity reaches the maximum near the drill column. Moreover, in the area between the well wall and the drill rod, the lower annular tangent flow rate is the largest, while the lowering speed of upper circulation flow velocity is relatively slow. As can be seen in Figure 6, the maximum

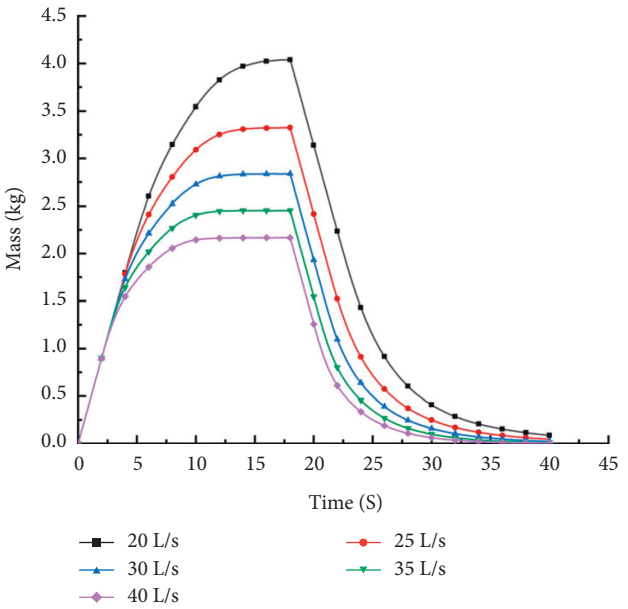

Figure 8: Curve of cuttings quality change at different displacement rates.

flow velocity zone is crescent-shaped and deflected at an angle with the rotational speed direction (clockwise). As can be seen from the streamline diagram, the drill rod eccentricity causes a spiral secondary flow vortex opposite the drill column rotation direction in the ring air. The secondary flow vortex scale increases with the rotation speed of the drill column as shown in Figure 7.

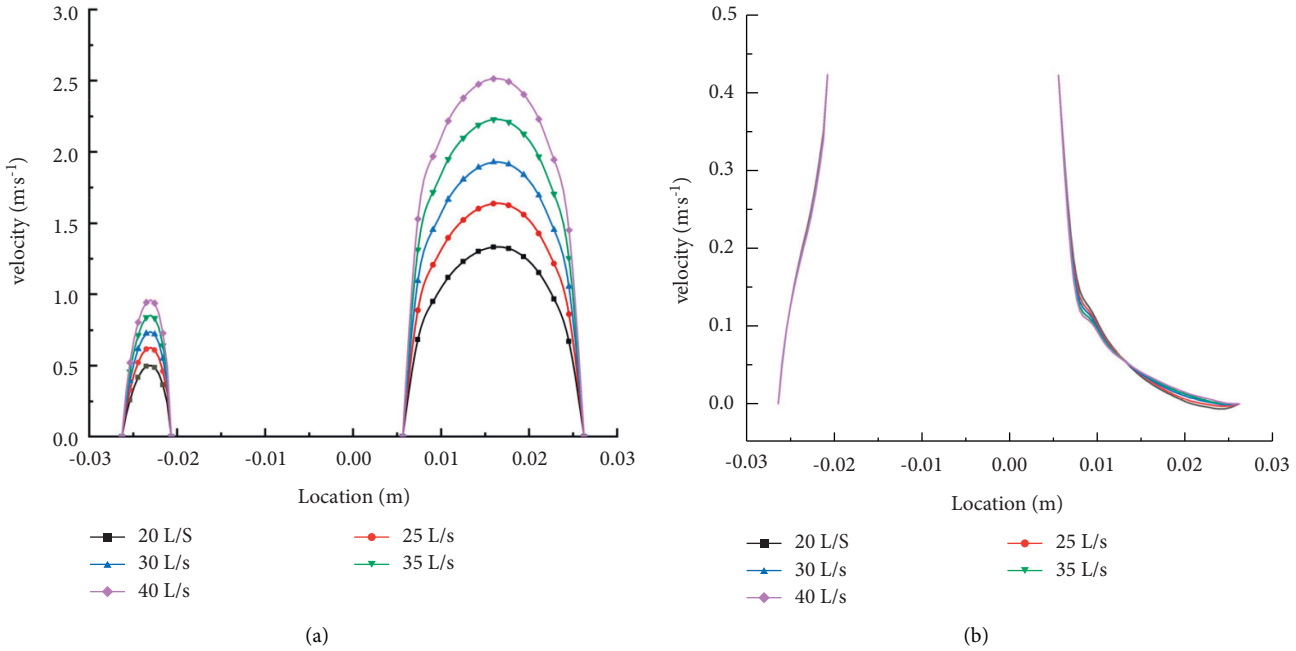

Figure 9: Curves of fluid velocity change at different displacement rates: (a) the axial velocity of the fluid; (b) maximum fluid velocity and its ratio.

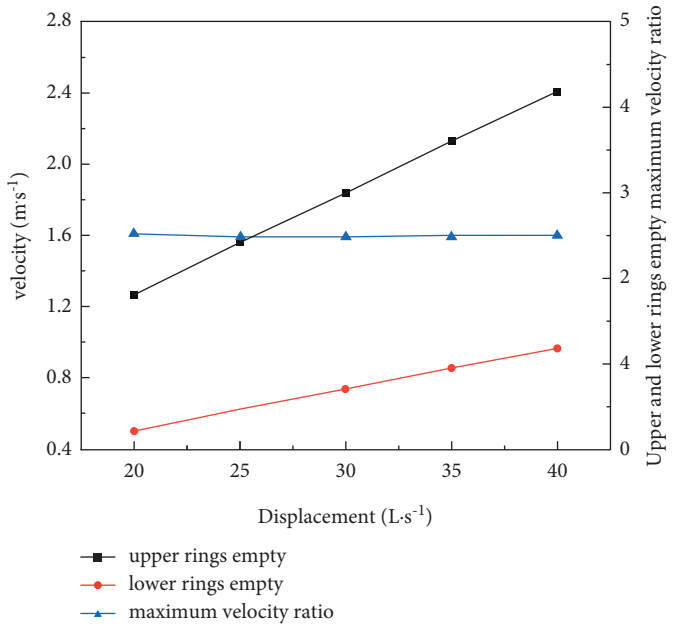

Figure 10: Curves of maximum velocity of the fluid and its ratio.

3.2. Effect of Drilling Fluid Displacement on Rock Debris Movement. Drilling fluid displacement is one of the critical factors affecting well hole debris settlement and well purification, and the rock carrying capacity and purification capacity of drilling fluid with different displacements are also different. To study the relationship between the debris deposition mass, purification time, and drill rod speed, this section simulates the influence on the debris settlement and purification time in the ring bore of the drilling fluid displacement in 20 L/s, 25 L/s, 30 L/s, 35 L/s, and 40 L/s, respectively. The other parameter settings are shown in Table 4.

Figure 8 shows the debris deposition mass and well hole purification time under different displacement. During drilling, with the gradual increase of drilling fluid displacement, the shorter the time in the linear settlement stage, the faster the transition settlement stage. Meanwhile, the faster the large displacement drilling fluid enters the dynamic stability phase, the curve slope of the debris mass

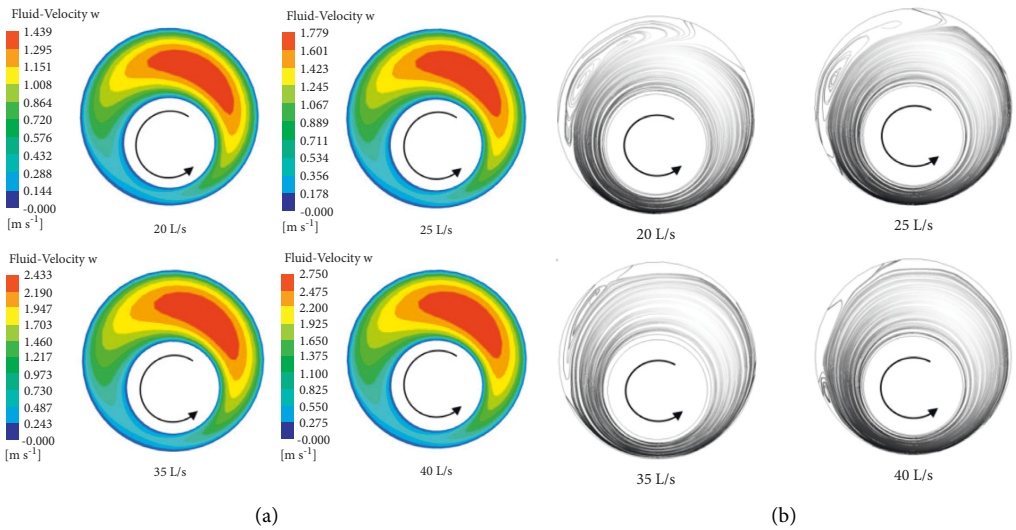

Figure 11: Cloud diagram of fluid velocity at different displacements: (a) speed cloud map; (b) streamlined diagram.

Table 5: Other parameters settings.

Rotation rate (rpm)	Output volume (L/s)	Eccentricity	Debris inlet flow rate (kg/s)
80	30	-0.6	0.45

changes the same during the transition settlement phase. This shows that increasing the drilling fluid displacement has a significant role in improving the rock carrying efficiency and makes the bore enter the dynamic stability stage quickly but has no impact on the time consumed in the transition settlement stage. At this time, the drill bit stops drilling and performs a reverse cycle operation, and then stops injecting chips after 18 seconds. Under different displacements, the curve slope and the curve curvature in the linear discharge phase are the same. Because the smaller the displacement, the amount of debris settled in the well eye, the longer the time required in the linear discharge phase, and the longer the time consumed by the well hole purification. It shows that improving the displacement of drilling fluid is beneficial to improving the efficiency of debris movement, reducing the debris amount and purification time in the well eye, and accelerating the stability of the flow field in the well eye.

As shown in Figure 9, it is evident that there is a velocity difference between the axial flow rates of the upper and lower rings, with the maximum and minimum flow rates increasing with the displacement. However, the change in the maximum velocity ratio is small, which shows that the increase of displacement has a great impact on the axial velocity of the fluid and less impact on the maximum velocity ratio of the upper and lower ring. Figure 10 shows the tangential flow velocity curve. The displacement has little effect on the maximum tangential velocity. It shows that the displacement can increase the fluid axial rock carrying capacity and reduce the amount of rock debris left in the ring air, but it has less impact on the tangential disturbance of the rock debris at the bottom of the ring space.

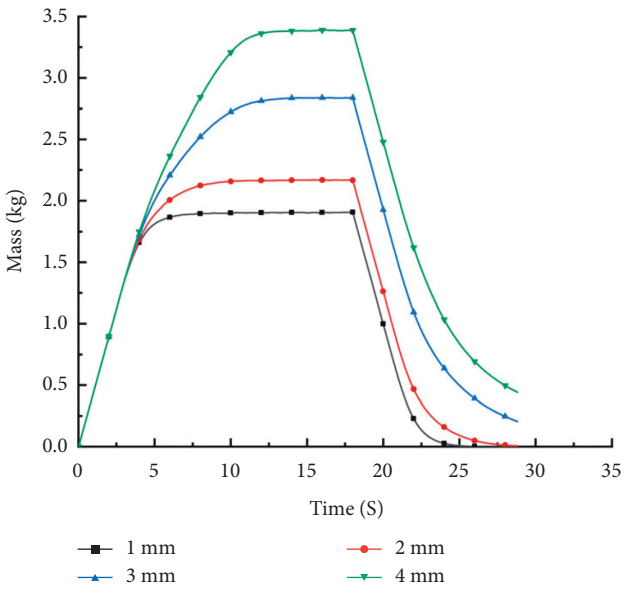

Figure 12: Rock debris mass change curve under different particle sizes.

As shown in Figure 11, the crescent shape in the maximum velocity zone does not change as the displacement increases. It can be seen from the streamline diagram that when other boundary conditions are certain, the secondary flow vortex scale decreases with the increase of the drilling fluid displacement, indicating that increasing the drilling fluid displacement can reduce the secondary flow vortex scale.

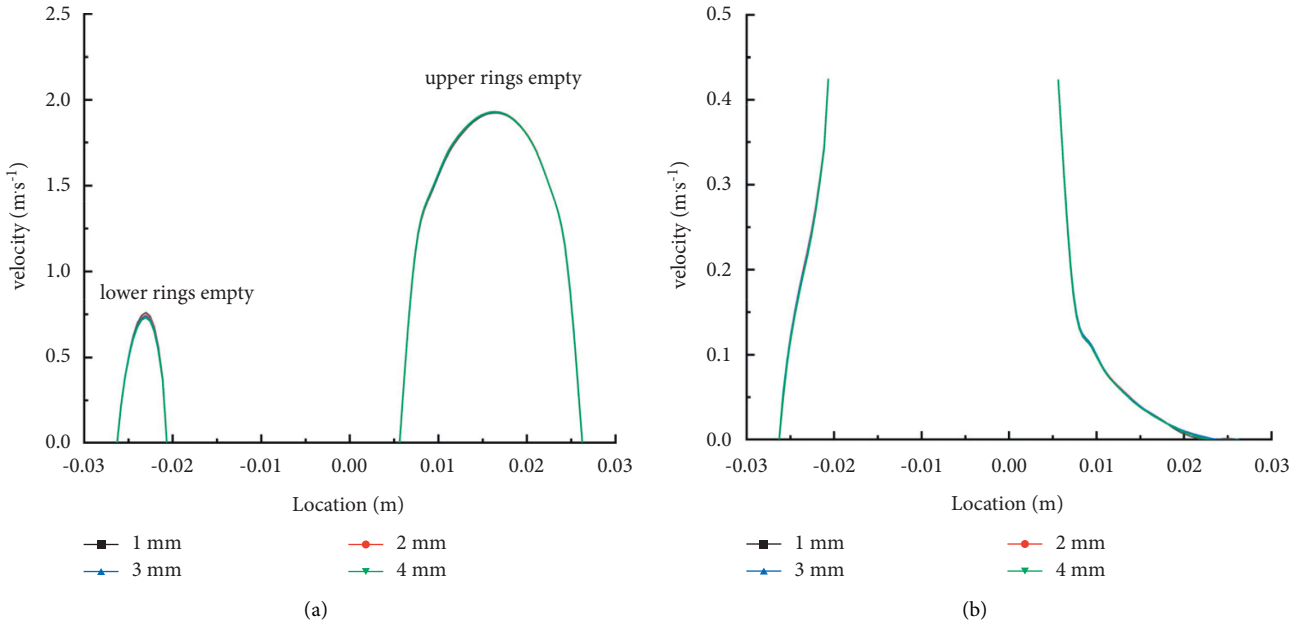

Figure 13: Variation curve of fluid velocity at different particle sizes: (a) the axial velocity of the fluid; (b) fluid tangential velocity.

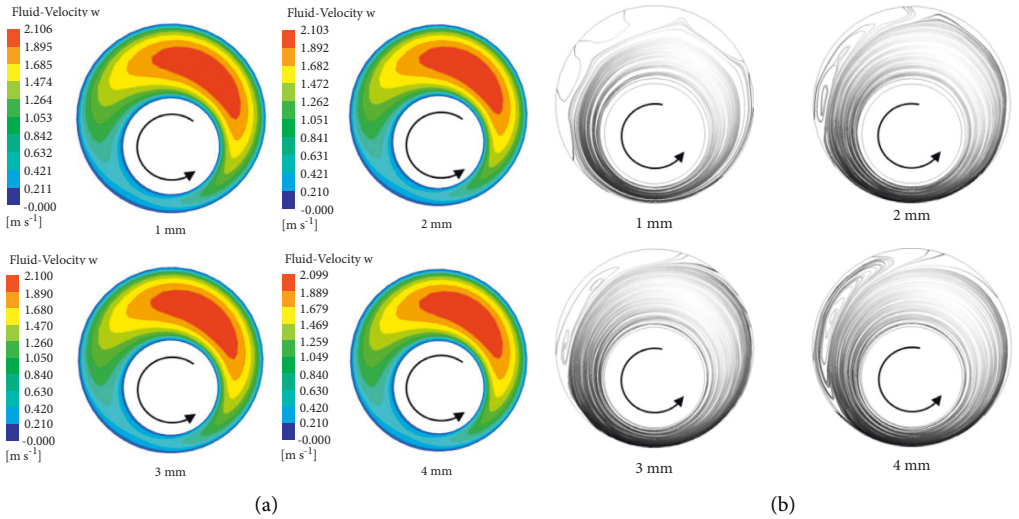

Figure 14: Cloud diagram of fluid velocity at different displacements: (a) speed cloud map; (b) streamlined diagram.

3.3. Effect of Debris Particle Size on Rock Debris Movement. In the drilling process, the debris particle size is generally a power distribution and Rayleigh distribution. Different debris particle sizes affect the rock carrying capacity and purification capacity. To facilitate the relationship of the debris deposition quality, purification time, and drill rod speed in the well hole ring, the debris particles in the well eye are set to the same particle size. This section simulates the effect on the settlement of rock debris and purification time in the condition of 1 mm, 2 mm size, 3 mm, and 4 mm, respectively. The other parameter settings are shown in Table 5.

Figure 12 shows the debris deposition quality and well hole purification time under different debris particle sizes. In the drilling process, with the gradual increase of the particle size of the drilling fluid, the time of the rock debris in the linear settlement stage has no impact. This indicates that it has entered the transitional settlement stage. However, the debris particle size greatly affects the transition settlement stage's curve slope, and the larger the particle size, the smaller the curve curvature. This shows that the small size rock debris can quickly make the bore enter the dynamic stability stage, but the particle size does not affect the time consumed in the linear settlement stage. When the drill bit stops drilling operation for reverse circulation operation, different debris particle sizes have less impact on the curve slope of the linear discharge stage and the curve of the excessive discharge stage. The larger the particle size, the greater the floating weight of the debris particles in the well eye, the easier it is to settle to the bottom of the ring space, the longer the time required for the linear discharge phase,

and the longer the time consumed by the well hole purification. It shows that small particles are beneficial to improving the efficiency of debris movement, reducing the debris amount and purification time in the well eye, and accelerating the stability of the flow field in the well eye.

Figure 13 shows a cloud diagram of the fluid flow velocity at different particle sizes. It can be seen from the figure that the particle size has little influence on the fluid axial flow velocity. Furthermore, when other boundary conditions are certain, the secondary flow vortex scale increases with the particle size, which shows that the particle size of small particles can reduce the secondary flow vortex.

As shown in Figure 14, it is obvious that there is a velocity difference between the axial flow velocity of the upper and lower rings. Still, the maximum velocity and minimum velocity change are very small, indicating that the debris particle size has little impact on the upper and lower rings' maximum velocity and tangential velocity.

4. Conclusion

According to the numerical simulation, this chapter mainly affects the debris settlement mass and fluid velocity in the eccentric ring of conventional steel drill. The main conclusions are as follows.

(1) By increasing the speed of the drill pipe, increasing the drilling fluid displacement, reducing the particle size, and reducing the eccentric degree can reduce the settlement of rock debris in the ring space;

(2) Due to the rotation of the drill rod, the annular fluid high-speed area, and the low-speed area deflection, resulting in the debris in the annular direction to the rotation direction, and a large number of debris gathered in the annular low-speed area;

(3) The more significant the rotation speed of the ring empty inside the drill rod is high, the displacement is small and the greater the eccentricity.

Data Availability

The datasets used and/or analyzed during the current study are available from the corresponding author on reasonable request.

Conflicts of Interest

The authors declared that they have no conflicts of interest.

References

[1] M. M. Huque, S. Imtiaz, S. Zendehboudi, S. Butt, M. A. Rahman, and P. Maheshwari, "Experimental study of cuttings transport with non-Newtonian fluid in an inclined well using visualization and electrical resistance tomography techniques[J]," *SPE Drilling and Completion*, vol. 36, no. 4, pp. 1–18, 2021.

[2] B. Amanna and M. R. Khorsand Movaghar, "Cuttings transport behavior in directional drilling using computational fluid dynamics (CFD)," *Journal of Natural Gas Science and Engineering*, vol. 34, pp. 670–679, 2016.

[3] J. O. Oseh, M. N. A. Mohd Norddin, I. Ismail, A. O. Gbadamosi, A. Agi, and A. R. Ismail, "Experimental investigation of cuttings transportation in deviated and horizontal wellbores using polypropylene-nanosilica composite drilling mud," *Journal of Petroleum Science and Engineering*, vol. 189, Article ID 106958, 2020.

[4] H. L. Zhang, G. S. Li, and Z. W. Huang, "Comment on experimental study of inclined debris migration," *Drilling process*, vol. 36, no. 05, pp. 13–17, 2013.

[5] X. Hengfu, S. Baojiang, and L. Hao, "Experimental study on debris movement in large displacement horizontal well section," *Petroleum Drilling Process*, vol. 3, pp. 1–6, 2014.

[6] K. Benyounes, A. Mellak, A. Flih, and Y. Azizi, "Study of cleaning the horizontal drains during the under balanced drilling well in the south Algeria fields," *IOP Conference Series: Earth and Environmental Science*, vol. 362, no. 1, Article ID 012035, 2019.

[7] M. Sorgun, A. M. Ozbayoglu, and M. E. Ozbayoglu, "Support vector regression and computational fluid dynamics modeling of Newtonian and non-Newtonian fluids in annulus with pipe rotation[J]," *Journal of Energy Resources Technology, Transactions of the ASME*, vol. 137, no. 3, Article ID 32901, 2015.

[8] M. Kamyab and V. Rasouli, "Experimental and numerical simulation of cuttings transportation in coiled tubing drilling," *Journal of Natural Gas Science and Engineering*, vol. 29, pp. 284–302, 2016.

[9] S. Akhshik and M. Rajabi, "CFD-DEM modeling of cuttings transport in underbalanced drilling considering aerated mud effects and downhole conditions[J]," *Journal of Petroleum Science and Engineering*, vol. 160, Article ID S0920410517304825, 2017.

[10] Y. J. Zhai, Z. M. Wang, and T. Y. Zhang, "Experimental study on movement of inflatable underbalanced drilling [J]," *Science Technology and Engineering*, vol. 16, no. 19, pp. 63–71, 2016.